A Micro Aircraft with Passive Variable-Sweep Wings

Songnan Bai, Runze Ding, and Pakpong Chirarattananon

Abstract—Traditional fixed-wing vehicles are equipped with multiple active aerodynamic surfaces for flight control. This inevitably necessitates several actuators, complicates the mechanical structure, and adversely impacts the flight efficiency, particularly for small aerial vehicles. As a lightweight and efficient solution, this work proposes to employ passive variable-sweep wings on a micro airplane to eliminate the need for active control surfaces while retaining effective pitch maneuverability. Depending on the thrust produced by the propellers, the wings passively sweep back and forth, relocating the center of pressure and affecting the pitch moment. The thrust-induced deformation substitutes the elevators for pitch control. Through aerodynamic modeling, the flight dynamics of the proposed vehicle is analyzed. The results show that the proposed design brings about amplified and accelerated pitch response. Lastly, a prototype was constructed to demonstrate and verify the enhanced aircraft's pitch control ability.

Index Terms—List of keyword: Aerial Systems: Mechanics and Control, Compliant Joints and Mechanisms, Underactuated Robots

Fig. 1. Photograph of the prototype with a closed-up photo of the elastic joint that governs the passive variable-sweep wing.

I. INTRODUCTION

MICRO aerial vehicles have been widely deployed for numerous applications, such as agriculture, search, rescue, communication, and surveillance. Among them, different aerial platforms feature unique advantages and drawbacks. Prevalently adopted multirotor vehicles enjoy a simpler mechanical design with precise, agile and highly versatile flight abilities [1]–[3]. In contrast, fixed-wing aircraft display more efficient flight but are unable to hover. Unlike multirotor vehicles, torque generation and attitude regulation of conventional fixed-wing platforms are usually accomplished through the use of ailerons (roll), elevators (pitch), and a rudder (yaw) [4]. Each of these active component requires an independent driver or actuator for control. For MAVs, miniaturized servomotors are often chosen for deflecting control surfaces [5], [6].

A number of recently developed fixed-wing MAVs depart from the traditional design, oftentimes featuring less distinctions between three types of control surfaces. Wingerons, for instance, are used to simultaneously control the pitch and

Songnan Bai, Runze Ding, and Pakpong Chirarattananon are with the Department of Biomedical Engineering, City University of Hong Kong, Hong Kong SAR, China (email: songnabai2-c@my.cityu.edu.hk;drunze2-c@my.cityu.edu.hk;pakpong.c@cityu.edu.hk).

the roll axes of a vehicle during flight [7]. Similarly, in [6], a pair of elevons were introduce to replace three kinds of three traditional control surfaces to render the vehicle maneuverable. These forms of mechanisms offer advantages for small aerial robots with limited payload and endurance as they cut down the number of required actuators and associated power expenditure. With the focus on reducing the mechanical and actuation complexity for lightweight fixed-wing MAVs, we propose an aircraft with passive variable-sweep wings. The proposed vehicle is equipped with a pair of motor-driven propellers as the main propulsion mechanism but totally devoid of other active control surfaces. This is accomplished by the use of non-actuated variable-sweep wings to enable the vehicle to retain its pitch control. The introduced mechanism enables the wings to passively change the sweep angle to relocate the position of the wing's center of pressure (CoP) with respect to the center of mass (CoM) to manipulate the pitch torque. When combined with an active yaw stabilizer by differential thrusts from two propellers, the vehicle is capable of controlling the pitch and yaw motion with only two actuators. Meanwhile, the roll degree of freedom is stabilized by the wing dihedral. The proposed configuration thoroughly eliminates active aerodynamic surfaces and associated actuators, significantly reducing the complexity and actuation requirements of the vehicle.

Previously, active variable-sweep wings have been incorporated into MAVs for improved flight maneuverability [8]–[11]. The added wing sweep in [9] enables the vehicle to operate at a high pitch angle and increases post-stall lift. In addition

to mentioned examples, active control of the wing sweep can be regarded as a form of wing morphing that changes the aerodynamics or CoP of the wings [8]. Applications of variable-sweep wings or other active wing morphing [12]–[14], therefore, enhance the performance and controllability of aerial vehicles. Our proposed vehicle differs from previous micro aircraft with morphing or variable-sweep wings as the wing deformation is passive as they are driven by the propelling thrusts. Yet, the vehicle with no active control surfaces retains the ability to proficiently manipulate its pitch dynamics as demonstrated herein.

This paper is organized as follows. In Section II, we outline a aerodynamic model for flat airfoils. Based on the model, the flight dynamics of robot and the equilibrium flight status are derived. Focusing on the longitudinal flight dynamics, the model elucidates how the passive variable-sweep wings assist and improve the pitch maneuverability of the robot. In Section III, we detail the design of the compliant joint and the fabrication of the vehicle. To verify the feasibility of the proposed mechanism and evaluate the pitch control performance, indoor and outdoor flight experiments are presented in Section IV. Lastly, conclusion and future works are discussed in Section V.

II. DYNAMICS OF AN AIRCRAFT WITH PASSIVE VARIABLE-SWEEP WINGS

In this paper, we propose an unmanned airplane that uses variable-sweep wings to achieve longitudinal flight path control. The novelty of the design is the passive or unactuated sweep mechanism. Unlike conventional swing wings with full controllability, the two wings of the proposed aircraft are effectively attached to the airframe via elastic revolute joints as shown in Fig. 1. Two motor-driven propellers are mounted at the aerodynamic center of the wings in the spanwise direction. With this design, both propellers not only play the role of propulsion to overcome the air drag and keep the vehicle flying, but also induce the torques to alter the wing sweep angles as shown in Fig. 1. The sweep changes the location of CoP of the wings and, therefore, influences the pitch dynamics of the vehicle.

To model the dynamics of the vehicle with passive variable-sweep wings, we focus on the longitudinal and pitch dynamics. For simplicity, flat rigid wings are employed as aerodynamic surfaces. In the following subsections, we determine the equilibrium pitch angle and flight path of the vehicle according to the propelling force to show that the uses passive joints improve the agility and pitch response of the aircraft when compared with a vehicle without variable-sweep wings.

A. Layout of the Aerodynamics Surfaces

To begin, we consider a particular configuration of a fixed-wing MAV that exhibits stable longitudinal (pitch and altitude) and lateral (roll and yaw) dynamics. The proposed vehicle employ a positive dihedral wing angle for passive roll stabilization while the pitch stability is accomplished by introducing a fixed horizontal stabilizer as a tail [15]. We have not introduce
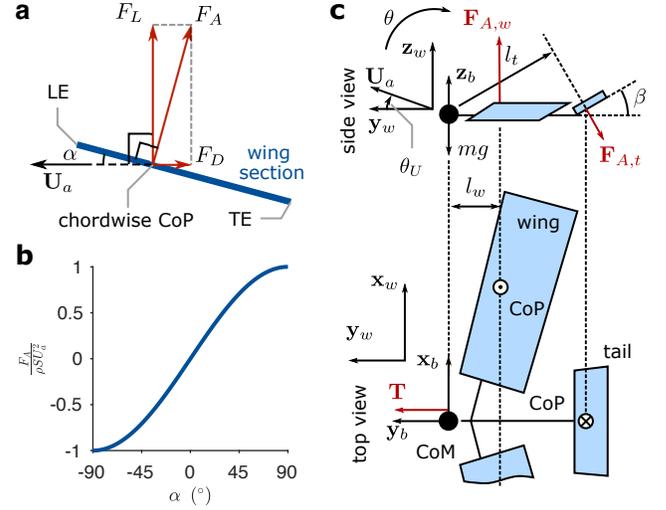
Fig. 2. (a) Lift and drag generated on a wing section with the angle of attack α. (b) Normalized aerodynamics force as a function of the angle of attack. (c) Force diagram of the aircraft in longitudinal flight. The figure shows the state when the body-fixed frame aligns with the world frame (pitch angle $\theta = 0°$).

the vertical stabilizer, instead, an active yaw controller using differential thrust is employed to achieve heading stable.

To describe the vehicle's configuration, we employ a body-fixed frame $(\mathbf{x}_b\mathbf{y}_b\mathbf{z}_b)$ located on the CoM with $\mathbf{y}_b$ being the frontal direction and $\mathbf{z}_b$ pointing upward. The robot is symmetric about the $\mathbf{y}_b\mathbf{z}_b$ plane. The two wings are mounted to the airframe with two linear-elastic revolute joints which allow the wings to sweep back and forth. The rotation axis of the elastic joint aligns with the normal vectors of the the wings lying in the $\mathbf{x}_b\mathbf{z}_b$ plane. This design keeps the dihedral angle of the wings constant even at different wing sweep angles. The placement of motor-driven propellers is arranged to assist the passive wing sweep such that the revolute joints are subject to torque proportional to that of the propelling thrusts. This allows the sweep angles to be indirectly controlled in flight by altering the thrust of the propellers as detailed in Section II-G (also visible in the supplementary video).

Unlike a regular airplane, as shown in Fig. 1, the tail of the proposed vehicle is fixed without elevators. The normal vector of the tail lies in the $\mathbf{y}_b\mathbf{z}_b$ plane pointing between positive $\mathbf{y}_b$ and $\mathbf{z}_b$ directions in order to generate the downward lift F_A in flight to stabilize the pitch motion as illustrated in Fig. 2c. Besides, the large separation between the two propellers enable the robot to generate significant yaw torque by applying differential thrust. This eliminates the need for an active vertical stabilizer for yaw control.

B. Aerodynamics of Flat Plates

First, we inspect the aerodynamic forces generated by the flat wings and tail. The lift and drag (F_L, F_D), acting at the CoP of the each aerodynamic surface, are given by

$$F_{L,D} = \frac{1}{2}\rho C_{L,D}SU_a^2, \tag{1}$$

where, ρ denotes the density of air, S denotes the area of the surface, lift and drag coefficients $C_{L,D}$ are functions of the

angle of attack α, and U_a denotes the norm of the translational velocity ($\mathbf{U}_a$) of the robot respect to the stationary air. Here, we assume the CoP of the wings or the tail are constantly located at the spanwise center of the aerodynamics surfaces. Lift F_L is perpendicular to the direction of the relative airflow velocity whereas drag F_D is opposite to the relative airflow as illustrated in Fig. 2a.

For flat aerodynamic surfaces present in the proposed vehicle, the lift and drag coefficients are provided by flat plate theory [16], [17] as

$$C_L = 2\sin(\alpha)\cos(\alpha) \quad \text{and} \quad C_D = 2\sin^2(\alpha). \quad (2)$$

Observe that flat plate theory indicates that the total aerodynamic force F_A always aligns with the normal vector of the surface as $F_D/F_L = \tan\alpha$ (see Fig. 2a). This property allows us to use the total aerodynamic force $F_A = \sqrt{F_L^2 + F_D^2}$ for modeling

$$F_A(\alpha, U_a) = \rho S \sin(\alpha) U_a^2 \quad \text{for} \quad \alpha \in [0°, 90°]. \quad (3)$$

Considering the expected symmetrical aerodynamics properties of the two side of a flat wing, it is reasonable to extend the domain to $\alpha \in [-90°, 90°]$ (see Fig. 2b). In addition, to account for the direction of F_A, we adopt a vector notation

$$\mathbf{F}_A = F_A \mathbf{N} = \rho S \sin(\alpha) U_a^2 \mathbf{N}, \quad (4)$$

where $\mathbf{N}$ denotes the normal vector of the wing. As a result, α is given by $90° - \arccos(\mathbf{N} \cdot \mathbf{U}_a/U_a)$.

C. Longitudinal Flight Dynamics

Prior to study the impact of the passive variable-sweep wings, we first inspect how the location of the wings affect the longitudinal flight dynamics. With the detailed flat plat theory, the proposed robot is abstracted as a rigid body with three massless flat aerodynamic surfaces (two wings and a tail) as shown in Fig. 2c.

To obtain the dynamics for the longitudinal motion, we ignore the lateral translational motion, the 2D translational dynamics of the aircraft with respect to the inertial frame (in $\mathbf{z}_w \mathbf{y}_w$) is first investigated given by

$$m\dot{\mathbf{U}}_a = R_\theta (\mathbf{T} + 2\mathbf{F}_{A,w} + \mathbf{F}_{A,t}) - \begin{bmatrix} 0 & mg \end{bmatrix}^\mathrm{T}, \quad (5)$$

where $\dot{\mathbf{U}}_a$ represents the translation acceleration of the vehicle, $R_{(.)}$ is a 2×2 rotation matrix, and $\mathbf{T} = [T, 0]^\mathrm{T}$ is the total thrust in the forward direction (generated by the two propellers). $\mathbf{F}_{A,w}$ and $\mathbf{F}_{A,t}$ are vectored aerodynamics forces applied on the two wings and the tail.

On the other hand, $\mathbf{x}_b$ axis of the robot is assumed to be always align with $\mathbf{x}_w$, leaving only the pitch rotational dynamics (a method commonly employed to isolate and analyze the longitudinal dynamics [5], [6], [16], [17]). To derive the pitch dynamics, we utilize the fact that forces produced by the two wings and the tail are perpendicular to the aerodynamic surfaces (flat plate theory). The total torque is attributed to the aerodynamic forces produced by the two wings $2F_{A,w}$, the tail

$F_{A,t}$, and a possible linear aerodynamic damping term.. This results

$$\ddot{\theta} I_x = -2l_w F_{A,w} - l_t F_{A,t} - b_\beta \dot{\theta}, \quad (6)$$

where the rotation of the robot about the $\mathbf{x}_b$ axis is prescribed by its pitch angle θ. I_x denotes the pitch moment of inertia, l_w and l_t are projected distances between the CoP of the wings and the tail and the CoM of the vehicle as depicted in Fig. 2c and b_β is a lumped damping coefficient.

Eq. (6) can be further expanded using the result from flat plate theory (Eq. (3)) to yield $F_{A,w} = \rho S_w \sin(\theta - \theta_U) U_a^2$. This is because the angle of attack of the wings α_w depends on the vehicle's pitch angle θ and the flight path angle θ_U as $\alpha_w = \theta - \theta_U$. For the tail, the surface is oriented at an angle β with respect to $\mathbf{y}_b$ as illustrated in Fig. 2c. Its angle of attack is $\alpha_t = \theta - \theta_U - \beta$. This results in $F_{A,t} = \rho S_t \sin(\theta - \theta_U - \beta) U_a^2$. For the proposed robot with the variable-sweep wings, l_w varies according to the wing sweep angle as detailed later in Section II-E.

D. Flight Equilibrium

In the following paragraphs, we investigate how the wing location l_w and thrust magnitude T influence the equilibrium flight state. This will subsequently enable us to visualize the impact of the passive variable-sweep wings as it will be shown that, for the proposed vehicle, l_w passively changes according to T.

To determine the equilibrium conditions, we reduce Eqs. (6) and (5) by imposing $\dot{\theta}, \ddot{\theta} = 0$ and $\dot{\mathbf{U}}_a = 0$. This results in

$$0 = \left(\frac{l_w}{l_t}\right) \sin(\theta - \theta_U) + \left(\frac{S_t}{2S_w}\right) \sin(\theta - \theta_U - \beta), \quad (7)$$

and

$$R_\theta^T \begin{bmatrix} 0 \\ 1 \end{bmatrix} = \begin{bmatrix} T/mg \\ 0 \end{bmatrix} + \frac{\rho 2 S_w U_a^2}{mg} \left(\begin{bmatrix} 0 \\ \mathrm{s}(\theta - \theta_U) \end{bmatrix} \right. \\ \left. + R_{\alpha_t}^T \frac{S_t}{2S_w} \begin{bmatrix} 0 \\ \mathrm{s}(\theta - \theta_U - \beta) \end{bmatrix} \right), \quad (8)$$

with $\mathrm{s}(\cdot)$ being a shorthand for sine. Assuming the nominal configuration of the relative tail-to-wing area of $S_t/(2S_w) = 0.15$ and the tail angle of $\beta = 30°$, Eqs. (7) and (8) are numerically solved to determine the equilibrium flight state $\{\theta_U, \theta, U_a\}$ at various wing sweep angles or wings' CoP locations (in terms of l_w/l_t). The results are shown in Fig. 3a to c. The plots are presented using dimensionless flight speed $U_a\sqrt{\rho 2 S_w/mg}$ and normalized thrust T/mg.

The obtained results provide several useful insights. For instance, $T/mg = 0$ corresponds to unpowered gliding or $\theta_U = 0°$ represents a horizontal flight path or cruising flight. Under these states, the pitch angle and flight speed can be determined. Another usage example is related to the impact of l_w/l_t. From Fig. 3a, it is possible to evaluate the configuration of l_w/l_t that lowers the thrust for level-flight ($\theta_U = 0°$). The optimal l_w/l_t is found to be 0.18, which minimizes T/mg to 0.34 (red stars in Figs. 3a to c). However, this most efficient configuration leads to a relatively low flight speed. On the other hand, to achieve the balance between range and efficiency, we
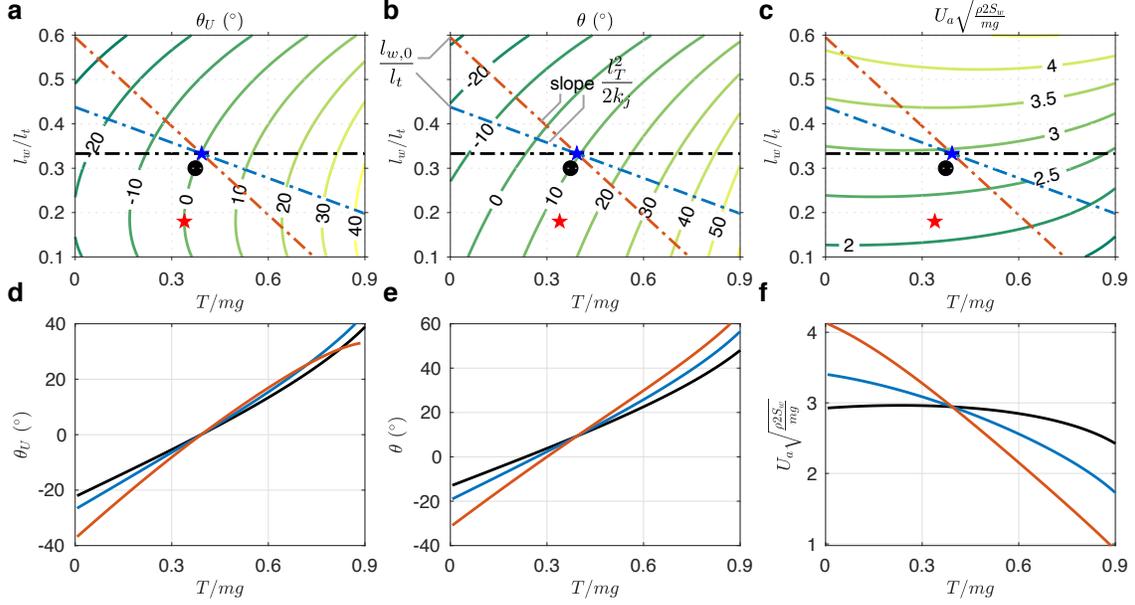
Fig. 3. The model predicted flight equilibrium states when $S_t/(2S_w) = 0.15$ and the tail angle $\beta = 30°$ under different T/mg and l_w/l_t. (a) to (c) show the equilibrium flight path angle, pitch angle and the dimensionless flight speed. The red stars represent the configuration for improved endurance. The blue stars represent the configuration for improved range. The black, blue and red dotted lines illustrate the working regions of the vehicle with different wing stiffness. (d) to (f) show equilibrium flight path angle, pitch angle and the dimensionless flight speed over different thrust conditions of the three example configurations.
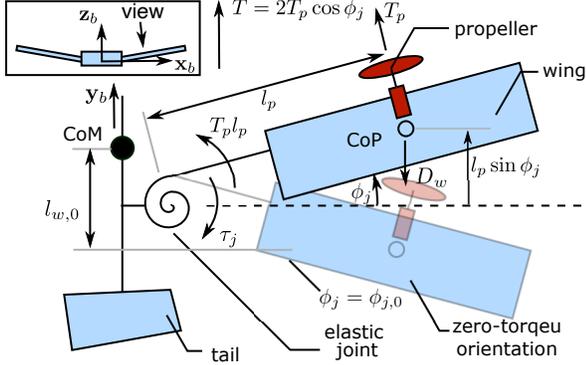
Fig. 4. Diagram highlighting the passive variable-sweep wings (only the right wing is shown). The figure is viewed from the direction normal to the surface of the right wing.

seek to find l_w/l_t that maximizes $U_a\sqrt{\rho 2S_w mg}/T$. In this case, the optimal l_w/l_t is 0.33 (blue stars in Figs. 3a to c).

In the next section, we explore how a passive mechanism could be incorporated such that the wing CoP, and therefore, l_w can vary according to the total thrust T. The use of passive mechanism noticeably affect the dynamics and the sensitivity of the aircraft.

E. Modeling of the Passive Variable-Sweep Wings

As outlined above, the introduction of elastic joints allows the vehicle to alter the wing sweep angles by adjusting the propelling thrust T. This subsequently changes the relative location between the CoM of the aircraft and the CoP of the wings, impacting the pitch torque and the equilibrium state.

To capture the behavior of the variable-sweep wings, we regard the variable-sweep mechanism as a compliant revolute joint with a linear elastic profile. Defining the wing sweep angle ϕ_j to be zero when the propeller points forward and positive for a frontal sweep as depicted in Fig. 4, the restoring torque induced by the compliant joint is

$$\tau_j = k_j(\phi_j - \phi_{j,0}),\qquad(9)$$

where k_j denotes the elastic constant and $\phi_{j,0}$ is the (negative) resting angle.

In equilibrium, τ_j is balanced by the moment created from the propelling thrust. This is because the aerodynamic force $\mathbf{F}_{A,w}$ is perpendicular to the wing surface and parallel to the joint axis, contributing to no zero net torque. For the contribution from the thrust of each propeller T_p, the torque magnitude is $T_p l_p$ (see Fig. 4). Furthermore, the frontal thrust T defined with Eq. (5) differs from $2T_p$ as the propellers' directions depend on the sweep angle ϕ_j, rendering $T_p = T/(2\cos\phi_j)$ (assuming negligible difference between left and right propellers). Therefore, in equilibrium, the wing sweep angle is acquired from the torque balance condition

$$k_j(\phi_j - \phi_{j,0}) = \frac{Tl_p}{2\cos\phi_j}.\qquad(10)$$

In other words, the sweep angle ϕ_j is dependent on T. Next, we examine how ϕ_j affects the location of the wing's CoP or l_w. This begins by defining the nominal distance of l_w as $l_{w,0}$ to be the value of l_w when the wing is resting at the original angle $\phi_{j,0}$. Using Fig. 4, it follows that l_w can be computed from ϕ_j as

$$l_w = l_{w,0} - l_p(\sin\phi_j - \sin\phi_{j,0}),\qquad(11)$$

Lastly, to produce the mapping between T and l_w, Eqs. (10) and (11) are combined to eliminate ϕ_j. Furthermore, we apply small angle approximations, $\phi_j, \phi_{j.0} \ll 90°$. The result simplifies to $l_w = l_{w,0} - l_p^2 T/2k_j$ or

$$l_w/l_t = l_{w,0}/l_t - \left(l_p^2 mg/2k_j l_t\right)(T/mg), \qquad (12)$$

Eq. (12) implies that (i) l_w/l_t decreases with an increasing T as anticipated; and (ii) $l_{w,0}/l_t$ and $l_p^2 mg/2k_j l_t$ are two lumped coefficients that affect the joint properties.

F. Passive Variable-Sweep Wings and Equilibrium Flight

To study the influence of the passive variable-sweep wings on the flight equilibrium state, we consider three hypothetical vehicles with the same cruising condition with maximized $U_a \sqrt{\rho 2 S_w mg}/T$ (blue stars in Figs. 3a to c) as found earlier (Section II-D). The three variants are (i) rigidly mounted wings ($k_j \rightarrow \infty$); (ii) passive variable-sweep wings with moderate k_j ($mgl_p^2/2k_j l_t = 0.67$, $l_{w,0}/l_t = 0.60$); and (iii) passive variable-sweep wings with soft k_j ($mgl_p^2/2k_j l_t = 0.27$, $l_{w,0}/l_t = 0.44$). First, for fixed wings, increasing or decreasing the forward thrust T moves the equilibrium state along the black horizontal lines in Figs. 3a to c. The change simultaneously alters the flight path angle θ_U, pitch angle θ and speed U_a of the vehicle as captured by Figs. 3d to f (black lines). In contrast, when the aircraft is equipped with passive variable-sweep wings, adjusting T concurrently deflects ϕ_j and l_w. The linear relationship between l_w and T (l_w/l_t and T/mg) described by Eq. (12) is demonstrated in Figs. 3a to c (as blue and red dashed lines for the two values of joint stiffness). Compared to fixed wings, the use of compliant joints enlarge the range of achievable flight path angle, pitch angle, and airspeed of equilibrium flight as shown in Figs. 3d to f. Interestingly, the impact is more pronounced on the wings with moderate joint stiffness. This is due to the slope ($mgl_p^2/2k_j l_t$) of the red lines in the plots in Figs. 3a to c being more perpendicular to the contour lines. In summary, the results indicate that the use of a passive mechanism with suitable compliance extends the control authority of the vehicle in longitudinal flight.

G. Joint Compliance and Dynamic Response

In addition to the analysis of equilibrium flight states, this section study how the passive wing mechanism improves the dynamic response. The analysis is carried out based on the previous longitudinal flight dynamics after linearization around respective equilibrium conditions.

To quantify the response around the equilibrium state, we regard the change in thrust from the equilibrium condition ΔT as the input of the linearized system. The longitudinal dynamics described by Eqs. (6) and (5) is then linearized such that the change in the flight path angle $\Delta \theta_U$ is the output. Other quantities (such as U_a and θ) become internal states of a fourth-order single-input single-output system. After the linearization, the response of the system to a step input is assessed through its rise time (the time the system takes to get from 10% to 90% of the final steady-state value) and settling time (the time

Para.	Description	Value	Unit
ρ	density of air	1.2	kg.m^{-3}
m	mass of the robot	30	g
β	pitch angle of the tail	30	deg
S_t	area of the tail	44	cm^2
S_w	area of the two wings	165	cm^2
l_t	moment arm of the tail	11.5	cm
$l_{w,0}$	elastic joint coefficient	5.5	cm
b_θ	aerodynamic damping term	30	N.mm.s
l_p	spanwise dist. of the joint to CoP	16	cm
k_j	elastic joint constant	64	N.mm
I_x	pitch moment of inertia	18.9	kg.mm^{-2}
l_1	elastic joint parameter	1.0	cm
l_2	elastic joint parameter	7.0	cm
l_3	elastic joint parameter	0.5	cm
$l_{e,0}$	resting len. of the elastic element	4.0	cm
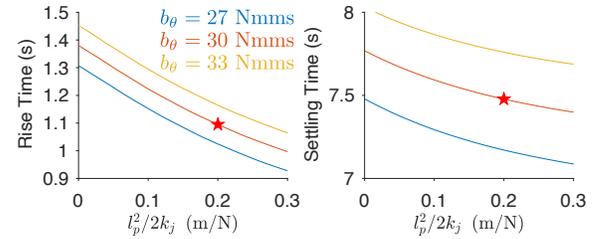
Fig. 5. The rise time and settling time of the linearized system under different elastic joint parameters.

it takes for the transient response to decay to within 2% of the final steady state. Shorter rise time and settling time indicate a faster system response.

To compute the rise time and settling time, we use numerical coefficients listed in Tab. I. Physical parameters used correspond to those of the fabricated prototype presented below. The inertia of the robot was estimated from CAD software. The pitch damping coefficient (b_θ) is approximated based on flat plate theory. Assuming the robot is rotating about the CoM with $\dot{\theta} = 1$ rad/s, b_θ is estimated by $\mathrm{d}\rho \left(2l_{w,0}^3 S_w + l_t^3 S_t\right) \dot{\theta}^2/\mathrm{d}\dot{\theta}$. With these parameters, the model predicts the equilibrium state for a cruising flight with $\theta = 9.0°$, $T = 0.11$ N and $\mathbf{U}_a = [5.66, 0]^\mathrm{T}$ m/s when $l_w = 3.3$ cm as marked by black dots in Fig. 3.

Fig. 5 plots the resultant rise time and settling time of the linearized dynamics as the joint stiffness k_j varies. At each value of k_j, the distance $l_{w,0}$ is respectively chosen to keep l_w at the cruising condition constant according to Eq. (12). Given that the estimate of b_θ maybe inaccurate, we provide the results for three values b_θ near the calculated value of 0.03 Nms. The results reveal that both rise time and settling time monotonically decrease as the passive joint softens. The impact is relatively substantial for the rise time but modest for settling time. Overall, compared to fixed wings, the passive variable-sweep wings reduce the response time. When combined with the improved flight envelope shown in Fig. 3, the passive mechanism thoroughly enhances the maneuverability of the aircraft.

III. PROTOTYPE AIRCRAFT

In this section, we start with the construction of the compliant joints for variable-sweep wings, followed by the manufacturing of the entire airplane.

A. Compliant Revolute Wing Joints

The mechanism for the proposed elastic joints, shown in Fig. 6a, is schematically illustrated in Fig. 6b. This linkage structure allows a linear elastic element to be used to simulate a revolute joint with a restoring torque proportional to the angular deviation, with the benefit of conveniently tunable stiffness. Fig. 6b displays the blue L-shaped component as the mechanical ground attached to the main airframe. Attached to the L-shaped ground via a revolute joint is the wing spar (yellow) that sits between two stoppers (grey) for limiting the motion range of ϕ_j to $\phi_- \le \phi_j \le \phi_+$ as shown in Fig. 6a and b. Note that ϕ_- is not necessarily $\phi_{j,0}$. The wing planform and the motor are mounted on the wing spar away from the revolute joint (not shown). A preloaded elastic element (rubber band) with original length of $l_{e,0}$ is installed at the tip of the L ground (as illustrated in Fig. 6a and b) and a location on the wing spar (defined by the distance from the revolute joint l_2, shown in Fig. 6a and b). The former location is characterized by distances l_1 and l_3 from the joint axis, perpendicular and parallel to the body axis y_b. Letting f_e be the restoring force produced by the elastic element, this configuration results in the joint torque of

$$\tau_j = l_2 f_e \sin \phi_e, \qquad (13)$$

ϕ_e is defined as the angle between the wing spar and the elastic element, which is dependent on the joint angle ϕ_j as

$$\phi_e = \tan^{-1}\left(\frac{l_2 \sin \phi_j + l_3}{l_2 \cos \phi_j - l_1}\right) - \phi_j. \qquad (14)$$

For simplicity, f_e is modeled according to Hooke's law with the stiffness k_e. It is proportional to the difference between the current length of the elastic element l_e and and the prestretched length $l_{e,0}$:

$$f_e = k_e \left(l_e - l_{e,0}\right), \qquad (15)$$

where l_e is also a function of ϕ_j

$$l_e = \sqrt{(l_2 \cos \phi_j - l_1)^2 + (l_2 \sin \phi_j + l_3)^2}. \qquad (16)$$

Substituting the results from Eq. (14) to (16) into Eq. (13) yields τ_j as a function of ϕ_j and $l_{e,0}$. For $l_{e,0} = 4.0$ cm and $l_1 = 1.0$ cm (Tab. I), τ_j varies with ϕ_j as plotted in Fig. 6c. The changes in l_3, and, in particular, l_2 affect the torque profile. Moreover, in the vicinity of $\phi_j = 0$, the restoring torque is approximately linear. Therefore, to approximate the result in to the form $\tau_j = k_j \left(\phi_j - \phi_{j,0}\right)$ introduced in the preceding analysis (Eq. (9)), the equation is linearized. The effective stiffness of the revolute joint k_j and the neutral angle $\phi_{j,0}$ are computed by linearizing Eq. (13) around the point $\phi_j = 0$. That is

$$k_j = \left. \mathrm{d}\tau_j\left(\phi_j\right)/\mathrm{d}\phi_j \right|_{\phi_j=0^\circ} \text{ and } \phi_{j,0} = \left. \tau_j\left(\phi_j\right)\right|_{\phi_j=0^\circ}/k_j. \qquad (17)$$
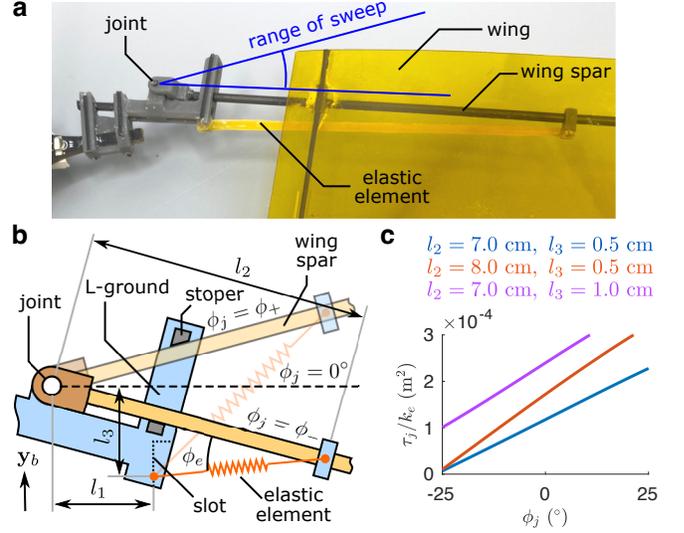
Fig. 6. (a) Close-up view of the passive variable-sweep wing joint. (b) A diagram of the elastic joint mechanism (right hand side, top view). (c) Numerically calculated torque profile of the three example elastic joint with different elastic element installation (different l_2 and l_3).

As observed Fig. 6c, the gradient or k_j can be easily manipulated in practice altering l_2 or shifting the mounting location of the elastic element along the wing's leading edge. Meanwhile, $\phi_{j,0}$ (the point where the lines in Fig. 6c intercept the horizontal axis) is primarily influenced by l_3. Therefore, compared to directly using a revolute spring, the benefit of the proposed design is the ability to tune the effective joint stiffness k_j by adjusting the lengths l_2 and l_3. For the actualized design, $l_2 = 7.0$ cm and $l_3 = 0.5$ cm (Tab. I). This results in $k_j = 64$ Nmm and $\phi_{j,0} = 28°$.

B. Prototype Fabrication

Apart from the customized variable-sweep wing mechanism, the vehicle consists of an airframe, pair of wings, a fixed tail, and flight avionics (Crazyflie 2.1 controller board with a 250 mAh Li-ion battery). The wings as well as the tail were made from 100-μm polyimide film (Kapton, Dupont) laser cut to the desired sizes (Epilog Mini 24). Wing spars and ribs (carbon fiber rods with 1.8 and 1.0 mm diameters) act as the leading edge and structural support to keep the wings and the tail flat. The wings and the tail were affixed to the airframe using 3D printed fixtures (Grey Resin, Form 3, Formlabs) through the elastic joints mechanism. For propulsion, we employed two 7×20-mm counter-rotating coreless DC motors with 40-mm 4-blade propellers. Prior to flight experiments, we identified the linear map between the motor command and the resultant propeller thrust using a static benchtop setup and a loadcell (ATI nano 25, The thrust of propeller is amplified by a moment arm).

IV. EXPERIMENTAL VALIDATION

A. Implementation

The aircraft was programmed with the yaw controller that utilizes the onboard gyroscope for feedback to minimize the

yaw rate of the vehicle through differential thrust commands. Roll was not actively controlled thanks to the dihedral wings. The communication between the vehicle and the ground station was achieved using Crazyradio PA. To assist the flight experiments, we constructed a catapult-assisted launch platform to provide an initial speed for the vehicle so that it enters an equilibrium state faster. With the launch platform, we preformed short-distance flight experiments in a $7 \times 3 \times 2.5$-m indoor environments and long-distance flight experiments outdoor.

B. Indoor Flight

The indoor experiments were conducted to evaluate the flight equilibrium state and the function of the passive variable-sweep wings. To track the trajectory and the wing sweep angle, a motion capture system (OptiTrack) with the range of $3 \times 3 \times 2.5$-m was employed and the vehicle was fitted with reflective markers on the two wings as visible in Fig. 1. In the experiments, the robot together with the launch platform (for providing initial takeoff speed) were initially placed at a location 4 m outside the region covered by the motion capture system (mocap). When launched, the thrust command was transmitted to the robot. Soon after the launch, the aircraft flew into the mocap region and the flight data were recorded.

In the experiments, we employed four vehicle configurations: two with variable-sweep wings and two with rigidly fixed wings (at $\phi_j \approx -10°$ and $-20°$). For each configuration, the robot was commanded to fly with several constant thrust levels (from 150 to 220 mN). In total, 48 trials were carried out. Despite being limited by the travel distance of ≈ 7 m, the launch platform accelerated the vehicle to 4.0 ± 0.1 m/s ($\approx 80\%$ of the equilibrium speeds) within 1 m. We use the averaged θ_U, θ and ϕ_j at the last 0.2 s from the recorded data as the measured equilibrium states as shown in Fig. 7a. Inside the 0.2-second period, the standard deviations of θ_U, θ and ϕ_j for each sequence are less than $1.7°$, $2.7°$ and $0.7°$, verifying that the vehicles were in the equilibrium states. Fig. 7b shows the recorded time courses of θ_U, θ and ϕ_j of four example flights (marked with "$\times$" in Fig. 7a, also shown in the supplementary video). The figure verifies that θ_U, θ and ϕ_j remained constant in the last 0.2 s of flights. For the two prototypes with rigidly fixed wings (blue and green in Fig. 7), the sweep angle ϕ_j were constant irrespective of the thrust. In contrast, for prototypes with passive joints (red and yellow), the equilibrium ϕ_j increases approximately linearly with the motor thrust as predicted by Eq. (10).

With known geometric properties ($S_t/S_w = 0.15$, and $\beta = 30°$, see Tab. I), the collected data of θ_U and θ were employed to identify the lumped joint coefficients (defined in Section II-E) for each vehicle by minimize the sum of squared errors of predicted and measured values of θ_U and θ. For the prototypes with rigidly fixed wings, the coefficient $l_p^2 mg/2k_j l_t$ is zero as $k \to \infty$. The best-fitted lumped parameters generate the lines in Fig. 7 with the trends consistent with the measurements. It can be seen from both experimental data and fitted model predictions that the thrust level positively correlates with the flight path angle θ_U and the pitch angle θ, with stronger
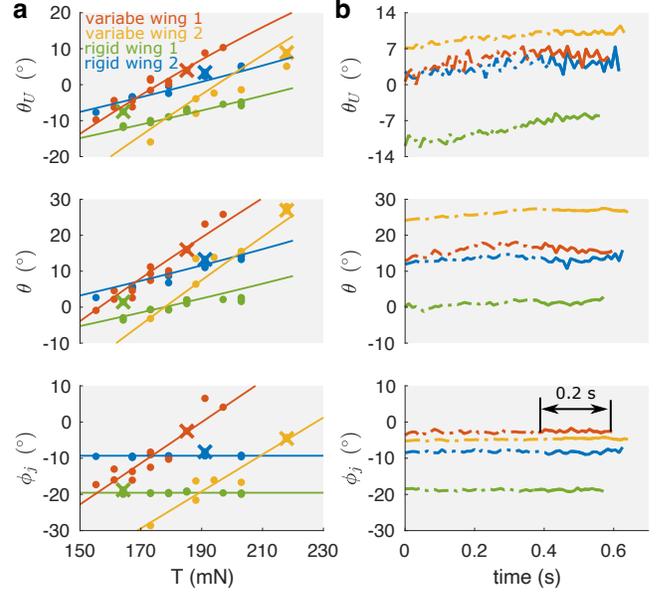
Fig. 7. Flight data from two vehicles with rigidly fixed wings and two with passive variable-sweep wings from the indoor experiments. (a) Averaged angles θ_U, θ and ϕ_j from the last 0.2 s of flights, representing the equilibrium state, are plotted against the thrust. The points denote the measurements and the lines represent the best-fitted models. (b) The time course of θ_U, θ and ϕ_j from four chosen flights (marked with crosses in (a)). The solid portions highlight the 0.2-s interval used for the calculation of the equilibrium values.

trends exhibited by vehicles with variable-sweep wings. This verifies the influence of the passive joints on the longitudinal dynamics.

In addition, more indoor flight demonstrations are provided in the supplementary video to directly compare the the vehicles with variable-sweep wings and rigidly fixed wings. The outcome is consistent with the numerical analysis from Fig. 3, validating the enhanced maneuverability in the pitch dynamics for robots with the passive variable-sweep wings.

C. Outdoor Flight

In addition to indoor flight, an outdoor flight was performed to display the robustness of the passive variable-sweep wings in practical environments and to verify the overall flight performance. Without the motion capture system, we were unable to capture the sweep angle and the attitude of the vehicle. Alternatively, two cameras were setup to capture and triangulate the flight trajectory of the vehicle from two views. This stereo vision setup allows the 3-D trajectory of the vehicle to be reconstructed using Matlab Computer Vision Toolbox.

The flight started from the launch platform at an altitude of ≈ 1 m. After being propelled from the launch platform, we applied the thrust with a step increase to instruct the vehicle to ascend. The thrust of the motors was increased from 179 to 224 mN at $t = 0.9$ s and lowered back to 179 mN at $t = 2.7$ s. The composited image of the flight and the reconstructed trajectory are shown in Fig. 8a and b. In flight, the vehicle climbed steeply after the brief increase in thrust and leveled off to an altitude of ≈ 3.5 m at the end. The flight path angle calculated from the flight trajectory clearly shows the upward
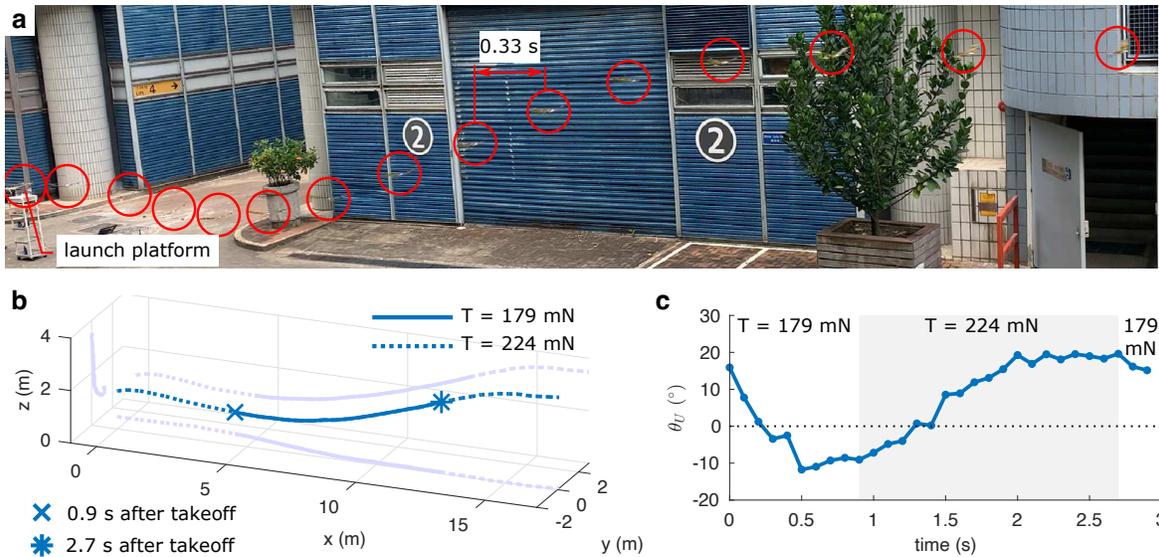
Fig. 8. (a) A composite photo taken from the the outdoor flight experiment. The robot is circled in red. (b) Reconstructed 3-D flight trajectory of the vehicle from the experiment. (c) The flight path angle of the vehicle.

and downward trends corresponding to the change in the thrust at 0.9 and 2.7 s as presented in Fig. 8c. The experiment illustrates the effective use of passive variable-sweep wings for pitch control.

V. CONCLUSION

In this work, we have proposed a passive variable-sweep mechanism for a small aerial vehicle. Leveraging simplified aerodynamic models, integrated with an appropriate abstraction of the passive joint mechanisms, we modeled and studied the flight dynamics of the proposed vehicle. The outcomes state that the passive variable-sweep wings enhance the range of achievable flight path and pitch angle of the robot and boost the response speed.

The prototype was constructed based on the derived analysis and resultant design guidelines. Findings from flight experiments verify that the mechanism with suitable design parameters eliminates the need for traditional elevators of fixed-wing aircraft for pitch control purposes. The vehicle with passive variable-sweep wings displayed amplified control authority, enabling the aircraft without elevators to climb or descend rapidly as intended.

REFERENCES

[1] Daniel Mellinger, Nathan Michael, and Vijay Kumar. Trajectory generation and control for precise aggressive maneuvers with quadrotors. *The International Journal of Robotics Research*, 31(5):664–674, 2012.

[2] Jing Shu and Pakpong Chirarattananon. A quadrotor with an origami-inspired protective mechanism. *IEEE Robotics and Automation Letters*, 4(4):3820–3827, 2019.

[3] Bingguo Mu and Pakpong Chirarattananon. Universal flying objects: Modular multirotor system for flight of rigid objects. *IEEE Transactions on Robotics*, 36(2):458–471, 2019.

[4] Federal Aviation Administration and United States. Federal Aviation Administration. *Pilot's handbook of aeronautical knowledge*. Skyhorse Publishing Inc., 2009.

[5] Andrei Dorobantu, Austin Murch, Bérénice Mettler, and Gary Balas. System identification for small, low-cost, fixed-wing unmanned aircraft. *Journal of Aircraft*, 50(4):1117–1130, 2013.

[6] Raghu Venkataraman and Peter Seiler. System identification for a small, rudderless, fixed-wing unmanned aircraft. *Journal of Aircraft*, 56(3):1126–1134, 2019.

[7] Ludovic Daler, Stefano Mintchev, Cesare Stefanini, and Dario Floreano. A bioinspired multi-modal flying and walking robot. *Bioinspiration & biomimetics*, 10(1):016005, 2015.

[8] Animesh Chakravarthy, Daniel T Grant, and Rick Lind. Time-varying dynamics of a micro air vehicle with variable-sweep morphing. *Journal of Guidance, Control, and Dynamics*, 35(3):890–903, 2012.

[9] Zachary R Manchester, Jeffrey I Lipton, Robert J Wood, and Scott Kuindersma. A variable forward-sweep wing design for enhanced perching in micro aerial vehicles. In *55th AIAA Aerospace Sciences Meeting*, page 0011, 2017.

[10] Julian Colorado, Antonio Barrientos, Claudio Rossi, and Kenny S Breuer. Biomechanics of smart wings in a bat robot: morphing wings using sma actuators. *Bioinspiration & biomimetics*, 7(3):036006, 2012.

[11] Louis Dufour, Kevin Owen, Stefano Mintchev, and Dario Floreano. A drone with insect-inspired folding wings. In *2016 IEEE/RSJ International Conference on Intelligent Robots and Systems (IROS)*, pages 1576–1581. Ieee, 2016.

[12] Benjamin Jenett, Sam Calisch, Daniel Cellucci, Nick Cramer, Neil Gershenfeld, Sean Swei, and Kenneth C Cheung. Digital morphing wing: active wing shaping concept using composite lattice-based cellular structures. *Soft robotics*, 4(1):33–48, 2017.

[13] Matteo Di Luca, Stefano Mintchev, Grégoire Heitz, Flavio Noca, and Dario Floreano. Bioinspired morphing wings for extended flight envelope and roll control of small drones. *Interface focus*, 7(1):20160092, 2017.

[14] Eric Chang, Laura Y Matloff, Amanda K Stowers, and David Lentink. Soft biohybrid morphing wings with feathers underactuated by wrist and finger motion. *Science Robotics*, 5(38), 2020.

[15] Eli Livne and Terrence A Weisshaar. Aeroelasticity of nonconventional airplane configurations-past and future. *Journal of Aircraft*, 40(6):1047–1065, 2003.

[16] Rick Cory and Russ Tedrake. Experiments in fixed-wing uav perching. In *AIAA Guidance, Navigation and Control Conference and Exhibit*, page 7256, 2008.

[17] Warren Hoburg and Russ Tedrake. System identification of post stall aerodynamics for uav perching. In *AIAA Infotech@ Aerospace Conference and AIAA Unmanned... Unlimited Conference*, page 1930, 2009.